Computational Materials Science 200 (2021) 110823

Contents lists available at ScienceDirect

Computational Materials Science

journal homepage: www.elsevier.com/locate/commatsci

Effect of heterostructure engineering on electronic structure and transport properties of two-dimensional halide perovskites

Rahul Singh [a], Prashant Singh [b,*], Ganesh Balasubramanian [c]

[a] Department of Mechanical Engineering, Iowa State University, Ames, IA 50011, United States
[b] Ames Laboratory, U.S. Department of Energy, Iowa State University, Ames, IA 50011, United States
[c] Department of Mechanical Engineering & Mechanics, Lehigh University, Bethlehem, PA 18015, United States

ARTICLE INFO

Keywords:
Density-functional Theory
Organic-inorganic halide perovskite
Bandgap
Electronicstructure properties
Transport properties

ABSTRACT

Organic-inorganic halide perovskite solar cells have attracted much attention due to their low-cost fabrication, flexibility, and high-power conversion efficiency. More recent efforts show that the reduction from three- to two-dimensions (2D) of organic–inorganic halide perovskites promises an exciting opportunity to tune their electronic properties. Here, we explore the effect of reduced dimensionality and heterostructure engineering on the intrinsic material properties, such as energy stability, bandgap and transport properties of 2D hybrid organic–inorganic halide perovskites using first-principles density functional theory. We show that the energy stability of engineered perovskite heterostructures is significantly enhanced. The heterostructures with improved stability also show excellent transport properties similar to their bulk counterparts. These layered chemistries demonstrate the advantage of a broad range of tunable bandgaps and high-absorption coefficient in the visible spectrum. The proposed 2D heterostructured material holds potential for nano-optoelectronic devices as well as for effective photovoltaics.

1. Introduction

Over the last decade, perovskites have been one of the most intensely examined classes of materials because of their outstanding optoelectronic properties [1–6]. The versatility of these materials encompasses a series of optoelectronic devices such as light-emitting diodes [1,2], transistors [3], lasing applications [4], as well as other intriguing electronic properties [5–11]. In particular, organic–inorganic halide perovskites (OIHP), archetypically $CH_3NH_3PbX_3$ (X = Cl, Br or I), have attracted significant attention because of their remarkable photovoltaic properties [12–14], achieving power conversion efficiency as high as 22.1% [4]. Thin OIHP films that are typically synthesized and examined for the electronic transport, suffer from stability issues. A potential solution is to employ planar heterostructures in lieu of the 3-dimensional (3D i.e., bulk) films [13,15–23]. Quantum confinement effect in two-dimensional (2D) chemistries [24] increases the bandgap due to a blue shift that decreases with increasing number of layers in a heterostructured material [25–28]. The decrease in bandgap due to increasing number of inorganic layers is detrimental to the stability of the heterostructure.

Recently, there has been a renewed interest in thermoelectric properties of halide-perovskites, which was motivated by the realization that complexity at multiple length scales can lead to new transport mechanisms in high performance perovskite materials. Theoretical predictions suggest that the thermoelectric efficiency could be greatly enhanced by quantum confinement [29] due to heterostructure engineering [30,31]. The formation of heterostructures by chemical layer deposition has been attempted to enhance photoluminescence [32], charge-transfer mechanism [33], and surface dopants [33]. The chemical layer deposition can lead to quantum confinement (QC) of charges. The decreasing dimensionality with QC aids in narrowing down electron energy bands, which produces high effective masses and Seebeck coefficients. Moreover, similar sized heterostructures decouple the Seebeck coefficient and electrical conductivity by electron filtering [34] that could result in an improved thermoelectric energy conversion.

In this work, we employed first-principles density functional theory (DFT) to examine the energy stability, electronic-structure, transport and optical properties of [001] terminated 2D OIHPs [35]. The 2D assemblies of $MAPbI_3$ (MA = CH_3NH_3) were created from the bulk OIHPs and stacked on monolayer (ML) MoS_2 (MoS_2ML). The thermodynamic stability of these heterostructure assemblies was analyzed with respect to $MAPbI_3$ layer distance from monolayer MoS_2 (MoS_2ML). This study

---

* Corresponding author.
E-mail address: psingh84@ameslab.gov (P. Singh).

https://doi.org/10.1016/j.commatsci.2021.110823
Received 5 July 2021; Received in revised form 16 August 2021; Accepted 20 August 2021

reveals that heterostructure of 2D-$MAPbI_3$ engineered with 2D-MoS_2 remarkably improves the thermodynamic stability of OIHPs. A detailed electronic-structure, bandgap, and transport properties study were performed on thermodynamically stable $MAPbI_3$ML/MoS_2ML hetero-assembly. A direct bandgap within the optimal range does not guarantee desired absorption in the visible range, therefore, understanding optical absorption also becomes critical in solar-cell materials for future applications.

2. Computational methods

2.1. Supercell generation.

We use relaxed 2D-MoS_2 unit cell (3 atom/cell) and relaxed 2D-$MAPbI_3$ (15 atom/cell) to construct a common supercell with 174 atoms (6C; 6 N; 36H; 12 Pb; 30 I; 28 Mo and 56 S atoms in the supercell). We generate a common cell in such a way that we can achieve minimum strain, less than 1%.

2.2. DFT Method.

We examine bulk and 2D variants of MA(Pb/Sn)I_3 OIHPs using first-principles density functional theory (DFT) [36,37] using the Vienna *ab initio* simulation package (VASP) [38–40]. We construct [0 0 1] terminated 2D OIHPs from 3D MA(Pb/Sn)I_3. For geometry optimization and electronic structure calculations, we use the projected augmented-wave (PAW) basis [38] and the Perdew–Burke–Ernzerhof (PBE) [40] exchange–correlation functional. We also use self-consistent GW potential functional of higher accuracy to establish the robustness of our predictions. The charge and forces are converged to 10^{-5} eV and 0.01 eV/Å, respectively, using energy cut-off of 800 eV. The Monkhorst-Pack [41] k-mesh grid of 7 × 7 × 3 is used for 2D $MAPbI_3$, 2D $MASnI_3$, and 3 × 3 × 5 for $MAPbI_3$ML/MoS_2ML. The tetrahedron method with Blöchl corrections is used to calculate the density of states (DOS) [38]. The thermoelectric properties are calculated using the BoltzTrap [42] code interfaced with VASP. The absorption spectra are calculated by obtaining the frequency dependent dielectric matrix as implemented within VASP [43].

3. Results and discussion

3.1. Cohesive and formation energies.

We calculate the cohesive energies using the van der Waals (vdW) density functional (vdW-DF), which correctly describes the vdW interaction in molecular complexes or solids at a reasonable computational cost [44,45]. We use a modified vdW-DF with the recently proposed rev-vdWDF2 [45,46]. The cohesive energy per atom was calculated as

$$E_c = E_{total} - \sum E_i^{isolated}$$

where energy (E_{total}) is calculated for the optimized heterostructures, E_c is the cohesive energy of the heterostructures with respect to constituent elements, where $E_i^{isolated}$ are the atomic energies of isolated with ‘i’ being the atom index. The cohesive energies were estimated both with and without vdW (dispersive potential) as shown in Table 1. Lower energy per atom in Table 1 with vdW shows that it has significant effect on heterostructure energies.

The formation energy (E_{form}) for the different heterostructures was calculated as

$$E_{form} = E_{total} - \sum E_i$$

where E_i is the ground state energy per atom (elemental solid) of the constituent elements in bulk form, where i = C (hexagonal), H (hexagonal), Pb (face-centere cubic), I (orthorhombic), S (orthorhombic) and Mo (body-centered cubic). The E_{form} of $MAPbI_3$ML/MoS_2ML at different interlayer distances is shown in Table 2. Evidently, $MAPbI_3$ML/MoS_2ML at z (=3.22 Å) is energetically most stable, therefore, we focused on z = 0 case in this work.

Table 1
Cohesive energies with and without vdW interaction for $MAPbI_3$ML/MoS_2ML.

System/E (eV/atom)	E_c	E_c(vdW)
MoS_2ML/$MAPbI_3$ML	−1.66E + 00	−4.60E + 00

4. Structural analysis of bulk and 2D variants of $MAYI_3$ (Y = Pb, Sn):

Hybrid organic–inorganic perovskites have an ABX_3 architecture, where A is a monovalent organic cation, $CH_3NH_3^+$ (i.e., MA^+), while B is a metal cation (i.e., Pb^{2+}, Sn^{2+}), and X is a halide anion (i.e., Cl, Br, I or their mixtures). In typical perovskite crystals, B occupies the center of an octahedral [BX_6] cluster [47], while A is 12-fold cuboctahedrally coordinated with X anions [15,48]. Generally, A does not directly play a major role in determining the band-structure, but its size is important. We construct a 2D structure (Fig. 1) by cutting through PbI_2 plane [0 0 1] of bulk $MAPbI_3$ and expose the PbI_2-terminated surface. We maintain the thicknesses of the slab to one monolayer along [0 0 1] and study the effect of heterostructure on the stability and electronic properties.

Here, we adopt the high temperature pseudo-cubic phase of $MAPbI_3$ [49,50]. The calculated (experimental) [51,52] lattice constants of bulk $MAPbI_3$ are a = 6.432 (6.361) Å, b = 6.516 (6.361) Å, c = 6.446 (6.361) Å, and $\alpha \approx \beta \approx \gamma \approx 90^\circ$. The predictions indicate a 3.41% increase in the simulated equilibrium cell volume relative to that in the experiments [51,52] with 1.27% increase in average Pb-I bond length. For 2D $MAPbI_3$, the calculated (experimental) lattice parameters of the PbI_2 surface are a = 6.437 (6.361) Å and b = 6.449 (6.361) Å respectively. We find a 1.38% increase in the lattice constant in [1 1 0] terminated surface of the simulated material, although the thickness of the slab shrinks by 2.5%. The reduced thickness (Fig. S1 (c), Fig. 1(a)) of the slab shrinks the overall volume by 1.33% relative to the bulk $MAPbI_3$ in the experiments.

The structural parameters of optimized MoS_2-deposited $MAPbI_3$ML are presented in Fig. 1. The $MAPbI_3$/MoS_2 monolayer supercell consists of 174 atoms/per unit cell (C = 6; N = 6; H = 36; Pb = 12; I = 30; Mo = 28; S = 56 atoms). The unit cell is periodic in the x-y plane and vacuum of at least 18 Å is maintained in the z-direction. The unit cell is constructed such that there is less than 1% mismatch between MoS_2 (2 atom per cell) and $MAPbI_3$ (12 atom per cell). We further relax the supercell to remove any residual strain from the unit cell construction due to lattice mismatch. The (X × Y × S) dimensions of the cell after relaxation are (6.362 Å × 38.567 Å× 30.741 Å). The optimized lattice constants a and b are 6.362 (6.361) Å and 6.428 (6.361) Å [53,54], respectively, similar to that of bulk $MAPbI_3$, shown in Fig. 1. Likewise, the average Pb-I bond length is 3.201 Å is similar to that in the bulk $MAPbI_3$. The distribution of Pb-I bond length tends to be uniform only for the bulk and the MoS_2ML deposited $MAPbI_3$. However, the change of Pb-I-Pb/I-Pb-I bond-angles in 2D and $MAPbI_3$ML/MoS_2ML are comparable with those of bulk $MAPbI_3$. To note, the bond lengths of Pb-I are substantially enhanced from bulk to 2D and longer than experimental (bulk) $MAPbI_3$. We notice 1.2% per formula unit volume decrease in optimized $MAPbI_3$ML/MoS_2ML compared to 2D $MAPbI_3$. The reduced volume leads to stronger intralayer hybridization. At the $MAPbI_3$ML/MoS_2ML interface, $MAPbI_3$ shows negligible polyhedral distortion in PbI_2, which suggests

Table 2
Formation energy (meV/atom) with varying $MAPbI_3$ layer distance from the MoS_2-layer, where z = 3.22 Å.

MoS_2-ML/$MAPbI_3$/z	z − 0.5	z	z + 0.5
E_f (meV/atom)	+39.100	−14.700	−0.393

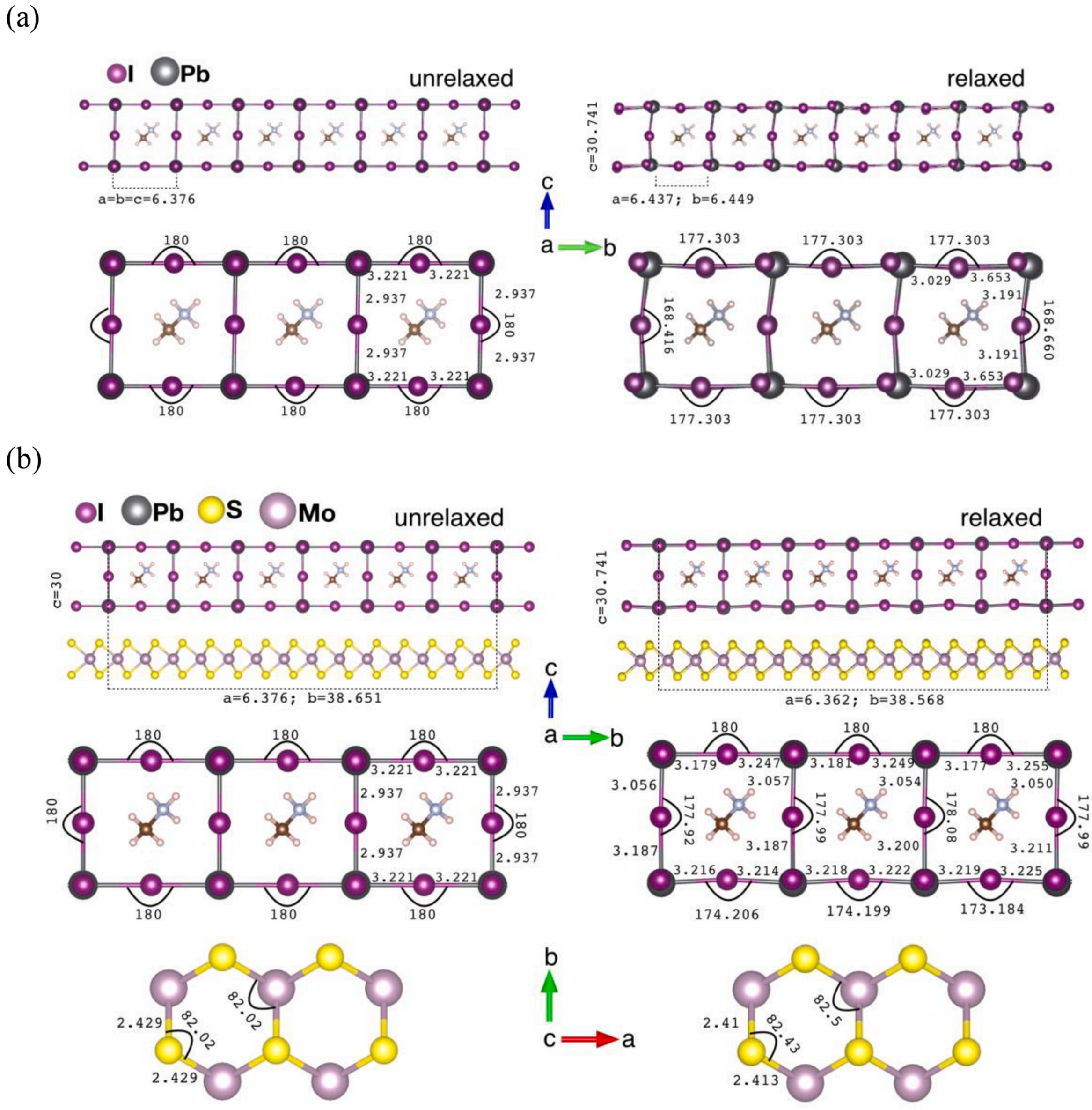

Fig. 1. The unrelaxed (left-panel) and optimized structure (right-panel) of (a) $MAPbI_3$ monolayer; and (b) $MAPbI_3ML/MoS_2ML$. The average bond-length and bond-angles of MoS_2ML changes from 2.428 Å (unrelaxed) to 2.412 Å (relaxed) and 82.02° (unrelaxed) to 82.5° (Mo-S-Mo)/82.43° (S-Mo-S), respectively.

of the structural stability of $MAPbI_3ML$ “on surface disposition”. This observation reveals that the $[PbI_6]^{4-}$ octahedra in layered structures account for optical and electronic changes for hybrid perovskite systems, as discussed later, and can be one of the reasons for the experimentally observed features such as a shifted band edge emission. The structural differences caused by MoS_2ML on $MAPbI_3ML$ deposition enhances the cohesive (binding) energies of the system as noted in Fig. 2.

Electronic properties of bulk and 2D variants of $MAYI_3$ (Y = Pb, Sn): Experimentally, the bandgap of cubic $MAPbI_3$ is ~1.5–1.62 eV [7]. Standard PBE calculations predict that bulk $MAPbI_3$ is a semiconductor with a direct bandgap of 1.73 eV, which agrees reasonably well with the experiments. The additional band-structure calculations of 2D $MAPbI_3$ in Fig. 3 indicate that both the 3D and 2D materials have a direct bandgap with the conduction band minimum (CBM) and valence band maximum (VBM) located at the M point of the Brillouin zone. The energy states ranging from −3 to 3 eV are mostly contributed by Pb and I atoms, signifying their influence on the physical and chemical properties of these perovskites. Specifically, the states near the top of the valence band are dominated by I-*5p* and Pb-*6 s* states, while the conduction

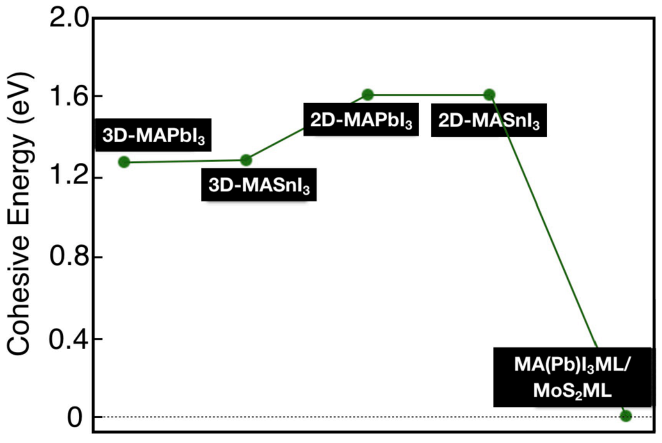

Fig. 2. The relative ordering of cohesive energies (eV) of bulk and 2D $MAPbI_3$ and $MAPbI_3ML/MoS_2ML$ (ML = monolayer).

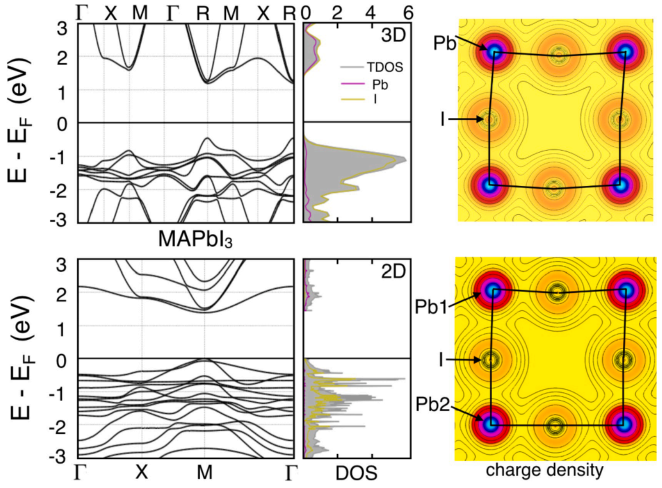

Fig. 3. Comparative band-structure, density of states (DOS) and (0 0 1) projected charge density of bulk and [0 0 1] terminated 2D $MAPbI_3$. Transitioning from bulk to 2D contributes to the DOS being more structured and the bands flatter. The bulk and 2D $MAPbI_3$ possess a calculated direct bandgap of 1.73 eV and 1.27 eV at R-point and M-point of Brillouin zone, respectively. The [0 0 1] projected charge density of 2D $MAPbI_3$ reveals enhanced bonding between Pb and I (highlighted by non-circular lobes both at Pb and I sites) compared to bulk. Identical isosurface values are employed for the charge density plots.

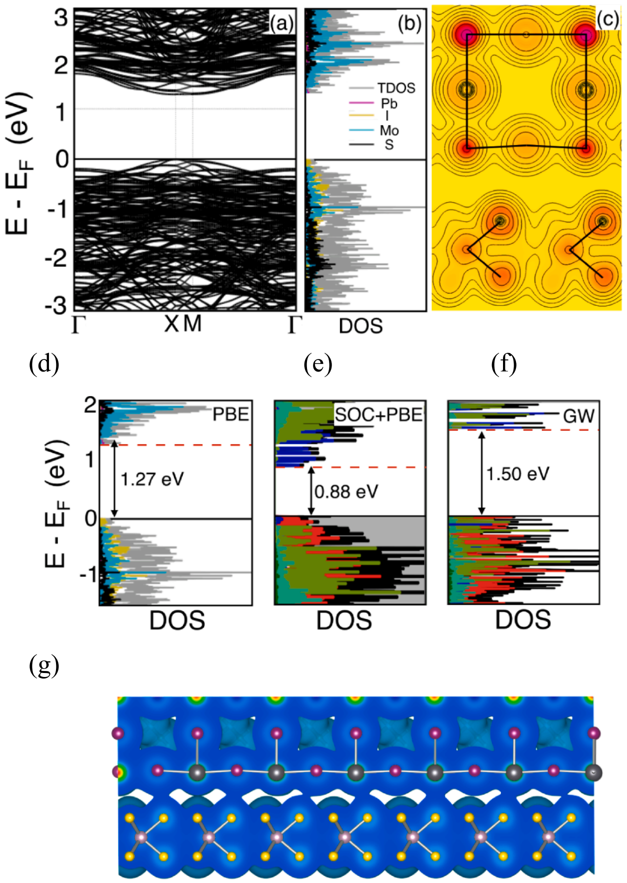

Fig. 4. (a) The electronic band-structure, (b) density of states, and (c) (1 1 0) projected charge density of 2D $MAPbI_3ML/MoS_2ML$. Additionally, (d) the PBE, (e) SOC + PBE DOS are compared with (g) GW DOS predictions. The bandgap predictions from GW are slightly improved over PBE. (g) The full charge-density from GW calculations are also illustrated (bottom-layer is MoS_2 while the top-layer is PbI_2).

bands are constituted by Pb-*6p* states with hybridization of I-*5p* states. As shown in Fig.S1, the surface terminated by PbI_2 contains more Pb atoms, which leads to a broader conduction band and thus a narrower bandgap of the 2D $MAPbI_3$ terminated by PbI_2.

For a deeper insight into the electronic properties of the heterostructured MoS_2ML, we compute the density of states (DOS), band-structure and (projected, full) charge densities for $MAPbI_3ML/MoS_2ML$, illustrated in Fig. 4a-f. The adsorption of $MAPbI_3ML$ introduces new flat energy levels between the valence and conduction bands of MoS_2ML resulting in a bandgap of ~1.27 eV in Fig. 4a,b. As the interactions between $MAPbI_3ML$ and MoS_2ML are weak, the band-structure of heterostructured MoS_2ML is effectively a combination of those of MoS_2ML and the adsorbed $MAPbI_3ML$. Hence, the bandgap reduction is attributed to the recombination of the energy levels from MoS_2ML and $MAPbI_3ML$. Nevertheless, for the 2D assembly, the new energy levels appear in the region of the conduction band, indicating that MoS_2ML can be tuned into a p-type semiconductor by doping with $MAPbI_3ML$. The DFT + PBE calculated charge density in Fig. 4c shows weak interaction between MoS_2 and PbI_2 layer.

As shown in Fig. 4a,b, the electronic states of $MAPbI_3ML$ in 2D $MAPbI_3ML/MoS_2ML$ are localized near the Fermi-level both in CBM and VBM. While the MoS_2 states in band-structure predominantly lies below −0.2 eV with respect to the Fermi level, E_F. The conduction bands with an energy range from ~1–3 eV is derived largely from the Pb-*s*/*p* and I-*s* states. The valence bands with a range from −3 eV – 0 eV exert strong hybridization between the Pb-*p*, I-*p*, Mo-*d* and S-*p* states. The localized distribution of electronic density on $MAPbI_3ML$ and MoS_2ML indicates that quantum confinement due to reduced dimension from bulk to 2D heterostructures leads to optimal bandgap and stability of $MAPbI_3ML/MoS_2ML$. In Fig. 4d,e, we show density of states calculated using PBE and PBE + SOC (SOC = spin–orbit coupling). The reduced bandgap of ~ 0.9 eV in SOC + PBE compared to PBE case arises from the annihilation of the Pb-s and I-p states due to SOC. Whereas GW (SOC) bandgap in Fig. 4f for $MAPbI_3ML/MoS_2ML$ is further improved to ~ 1.5 eV compared to PBE (1.27 eV) and PBE + SOC (~0.9 eV). The improved bandgap in GW calculation can be attributed to self-energy correction to Pb-s and I-p states. The charge density for $MAPbI_3ML/MoS_2ML$ calculated using DFT-GW are shown in Fig. 4g. Notably, a weak charge sharing from MoS_2 to PbI_2 layer was observed in contrast to 2D projected charge-density in Fig. 4c. The effective charge pulled from S (top atoms)-layer to Pb-I layer in GW calculation make sense due to high electronegativity of I.

In Table 3, we compare predictions of bandgaps calculated with PBE and GW functionals, where the GW + SOC predicted bandgap remains within the optimal region 1.2 to 1.8 eV. Notably, the MoS_2ML (2D) has a predicted direct bandgap of 1.73 eV as shown in Fig. 3 (bottom-panel), closer to the experimentally observed bandgap of 1.70 eV [55,56]. The VBM of MoS_2ML is contributed by Mo-*4d* and S-*3p* states, while the CBM is mainly due to Mo-*4d* states and feebly by S-*3p* states.

Thermoelectric properties of bulk and 2D variants of $MAYI_3$ (Y = Pb, Sn): A band-structure possessing a large-effective mass in CBM and with a minimum energy of about $5k_BT$ above the VBM, can potentially achieve nonmonotonic Seebeck coefficient, and hence a large thermoelectric power factor (*PF*) [57]. Deposition of $MAPbI_3ML$ on MoS_2ML introduces resonant states that can achieve a tailored band-structure. We determine the band effective mass m^* from the second order derivative

Table 3
Bandgap (in eV) of 2D $MAPbI_3$ and $MAPbI_3ML/MoS_2ML$ calculated with PBE, PBE + SOC, and GW (SOC), respectively.

System	Bandgap [eV]		
	PBE	PBE + SOC	GW
2D $MAPbI_3$	1.50	0.41	1.60
MoS_2-ML/$MAPbI_3$	1.31	0.88	1.54

of the band energy with respect to the wave vectors.

$$\left(\frac{1}{m^*}\right) = \frac{1}{\hbar^2}\frac{\partial^2 E_n}{\partial k_x \partial k_y}$$

where, x and y are the directions in reciprocal space, n is the band index, E_n is the band energy, and $\hbar$ is the modified Planck's constant. The derivatives are evaluated at CBM for electrons (m^e) and at VBM for holes (m^h). The reduction in dimensions from bulk to 2D creates opportunities to optimize the highly anisotropic structures due to the smaller directional effective mass (electrical conductivity$\sigma \propto \frac{1}{m^*}$) [58].

The calculated effective hole/electron mass for bulk MAPbI$_3$ is (0.17; 0.19; 0.28) m_h^* and (0.27; 1.51; 0.12)m_e^*, respectively. The three values in the parentheses represent the three perpendicular directions (x, y, z), while for 2D structures we consider the two planar directions (x, y). For 2D MAPbI$_3$, the corresponding values are (0.17; 0.33) m_h^* and (1.53; 0.85)m_e^*, respectively. The calculated effective mass for 2D MAPbI$_3$ indicates an obvious in-plane anisotropy due to [1 0 0] stacking. The strong directional effective mass is larger along [1 0 0] stacking, while along the direction orthogonal to the stacking [0 1 0] the computations predict smaller values. Thus, we deduce that the carrier mobility is high (small effective mass) along [0 1 0], with heavy mass states present in the transverse direction, i.e., [1 0 0]. In MAPbI$_3$ML/MoS$_2$ML, the energy minima/maxima occur at the X [½ 0 0] point. The calculated hole- and electron-effective masses at M−point are $m_h^* = (0.76;\ 1.13)$ and $m_e^* = (3.40;\ 1.51)$, respectively. The large anisotropy in the effective mass along the [1 0 0] direction facilitates hole transport along [1 0 0] compared to the electrons. However, along the [0 1 0] direction, both electrons and holes have equal effective masses resulting in similar transport properties. As shown in Table 4, the effective mass in SOC case is slightly increased in X symmetry-direction, however, SOC shows slight reduced effective mass in M-symmetry point. Except M(x), the change in all other directions is negligible.

In thermoelectric (TE) materials, a high Seebeck coefficient (S) at a given carrier concentration results from a high overall DOS effective mass (m_d*). However, σ decreases with increasing m_d*, and also depends on the inertial effective mass m*. Ioffe showed empirically that a carrier concentration $n \sim 10^{18}$–10^{20}cm^{-3} is mostly satisfied for doped semiconductors corresponding to degenerate semiconductors or semimetals [59]. Here, we predict a similar range for n_{hole} and n_{electron}. As the doping concentration increases, σ increases and S decreases. Fig. 5 (a-c) present S predictions for 2D MAPbI$_3$ and MAPbI$_3$ML/MoS$_2$ML. In comparison with bulk MAPbI$_3$ [60], we find that S of 2D MAPbI$_3$ is ~20% lower. The large S in bulk MAPbI$_3$ arises from the DOS and band mobility. As shown earlier in Fig. 3, the DOS above and below the Fermi level have a significant contrast in the bulk structures^{53} compared to the 2D counterparts, and the smaller m* in 3D materials leads to an increased band mobility [60] that is important to enhance the electronic transport. In Fig. 5 (top panel), we show that bulk MAPbI$_3$ has marginally better TE properties than 2D MAPbI$_3$ and MAPbI$_3$ML/MoS$_2$ML as the contribution to the overall S depends on the number of positive and negative charge carriers. At lower temperatures the population of minority carriers is small, and their contribution to S is insignificant. Nevertheless, at higher temperatures, a broadening in Fermi distribution leads to an exponential increase in minority carrier conductivity, which reduces S.

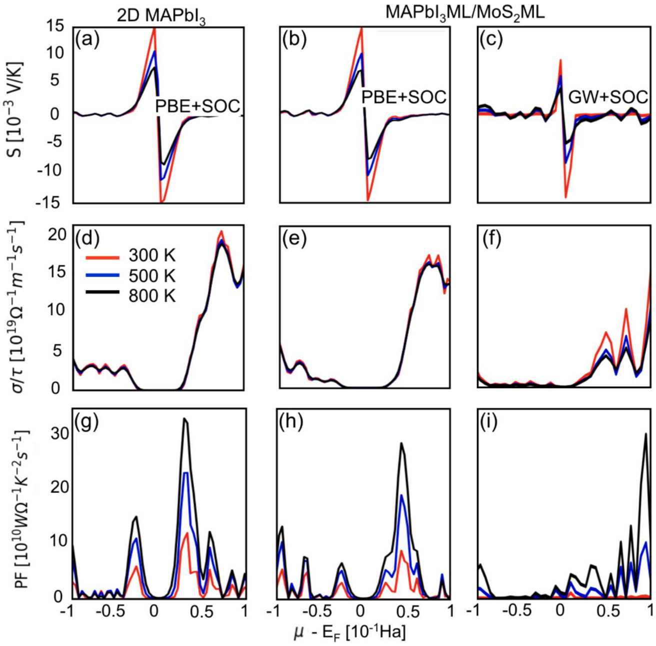

Fig. 5. The Seebeck coefficient (a, b, c), the electrical conductivity (d, e, f), and the power factor (g, h, i) of 2D MAPbI$_3$ (left-panel) and MAPbI$_3$ML/MoS$_2$ML (center and right panels) are shown at 300 K, 500 K and 800 K, respectively (ML = monolayer). The thermoelectric properties of MAPbI$_3$ML/MoS$_2$ML calculated using SOC + PBE (b, e, h) and SOC + GW (c, f, i) are also presented as a function of the chemical potential.

$PF = S^2\sigma$ of a TE material quantifies their electrical power generation ability. The most efficient TE materials possess high σ and high S. Since σ and S have competing dependencies on n, simultaneously obtaining high values for both properties is challenging. We compare the calculated PF per relaxation time as a function of temperature for MAPbI$_3$ML and that with MoS$_2$ML. Although both materials originate from the same parent cubic crystal structure, differences are noted in their TE properties (Fig. 5 (d)–(i)). The dissimilarities in σ of 2D MAPbI$_3$ and MAPbI$_3$ML/MoS$_2$ML originates from the intrinsic *sp*-type bonding of the heterostructure. The 2D OIHP deposited on MoS$_2$ has a lower $PF \sim 29.3 \times 10^{10}$ W/m.K^2.s relative to 2D MAPbI$_3$ (~32.5 × 10^{10} W/m.K^2.s) due to an enhanced conductivity [60]. Both 2D MAPbI$_3$ and MAPbI$_3$ML/MoS$_2$ML exhibit strong temperature dependence for S, but σ essentially remains temperature invariant. Thus, the PF predictions for specific chemical potential values at 800 K, Fig. 5(h) and (i), are ~100% and ~200% higher than at 500 K and 300 K, respectively, for both materials. Note that PF of 2D MAPbI$_3$ is ~10% higher than MAPbI$_3$ML/MoS$_2$ML, but the heterostructure has a significantly enhanced energetic stability. On one hand, OIHPs possess the advantage of hybridization, while on the other hand, their engineered geometries demonstrate the ability to tune TE properties through nanostructuring. In addition, the PF can be further controlled by the concentrations of the ionic dopants.

Absorption spectra of MAPbI3/MoS2ML: In Fig. 6, we display the computed optical absorption spectra for the energetically stable MAPbI$_3$ML/MoS$_2$ML heterostructure. The absorption spectra of the direct bandgap MAPbI$_3$ML/MoS$_2$ML is compared against that of two highly

Table 4
Effective mass (in units of m$_o$) of MAPbI$_3$ML/MoS$_2$ML with and without spin–orbit coupling.

	NON-SOC				SOC			
	X		M		X		M	
	x	y	x	y	x	y	x	y
Valence	0.759	1.127	3.838	0.183	0.902	1.702	1.666	0.981
Conduction	1.510	3.399	0.056	1.350	1.945	2.539	0.023	1.311

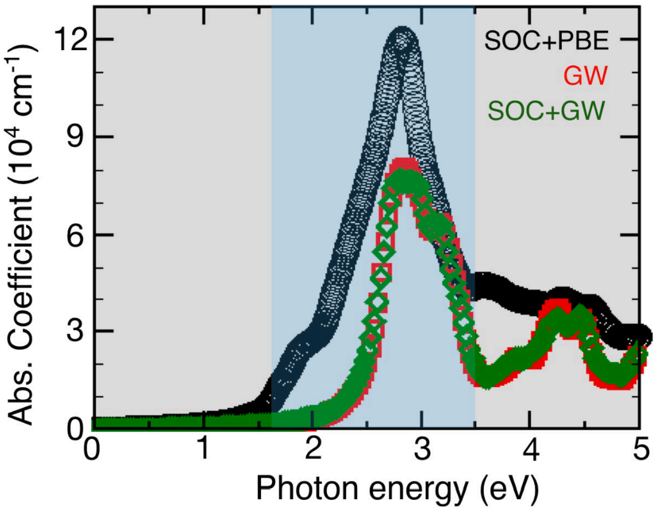

Fig. 6. The calculated optical absorption spectra of the energetically most stable $MAPbI_3ML/MoS_2ML$. The heterostructured material exhibits very high absorption coefficient in the visible range of light from 1.59 to 3.26 eV (shaded zone) compared to Si and bulk $MAPbI_3$ [58–60] Predictions from SOC + PBE, GW and SOC + GW calculations are compared. The GW, a higher accuracy functional, shows an insignificant decrease in the absorption coefficient.

efficient solar-cell materials, Si and $MAPbI_3$ [53,54,61] Amongst these, the computationally designed $MAPbI_3ML/MoS_2ML$ material exhibits a larger absorption coefficient in the visible-light range (from 1.59 to 3.26 eV) (for comparison, the optical absorption of Si and $MAPbI_3$ is elaborately discussed in Ref. [53,54,61]). Moreover, $MAPbI_3ML/MoS_2ML$ shows modest absorption in infrared range because of its smaller bandgap relative to the bulk $MAPbI_3$, indicating that majority of the total solar irradiance spectrum can be absorbed by $MAPbI_3ML/MoS_2ML$. These desirable properties render the heterostructured $MAPbI_3ML/MoS_2ML$ with the distorted perovskite chemistry as a very promising solar material with potential for high power conversion efficiency. The decomposition of $MAPbI_3$ when exposed to the ambient condition is a challenging issue, however, recent study by Fan and coworkers showed that $MAPbI_3$ thermally decomposes back to one crystal PbI_2 layer at a time driven by a surface dominated reaction [62]. The new understanding suggests that simple encapsulation with atomically thin 2D hexagonal boron nitride protects the top surface, which helps impeding the degradation of the underlying layers. Therefore, simply inhibiting the structural transitions of the surface layers using MoS2 capping by depositing on halide layers should greatly increase the overall structural and thermal stability.

5. Conclusion

In summary, we used density-functional theory methods to manipulate the electronic and thermoelectric properties of 2D organic–inorganic halide perovskites. Our study shows that a chemically deposited monolayer of 2D $MAPbI_3$ on a monolayer MoS_2 remarkably enhances the energetic stability and provides an optimal bandgap required for photovoltaic applications. The enhanced bandgap compared to bulk $MAPbI_3$ arises from the reduced dimensionality and increased quantum confinement effect in 2D heterostructures. Our computations also reveal that $MAPbI_3ML/MoS_2ML$ possesses excellent thermoelectric properties relative to bulk $MAPbI_3$ due to the intrinsic *sp*-type bonding of the heterostructure. The higher energy stability, suitable bandgap and better optical absorption makes $MAPbI_3ML/MoS_2ML$ a potential material for the high-efficiency perovskite solar cells. We propose that 2D materials with charge alternations, such as transition metal dichalcogenides, offer a method to encapsulate the perovskite films. We believe our predictions provide a useful guideline for future experiments examining the stability and photovoltaic properties of 2D perovskites deposited on layered substrates.

6. Data availability

The authors declare that the data supporting the findings of this study are available within the paper and supplement. Also, the data that support the plots within this paper and other finding of this study are available from the corresponding author upon reasonable request.

CRediT authorship contribution statement

Rahul Singh: Formal analysis, Writing – original draft, Writing - review & editing. **Prashant Singh:** Conceptualization, Formal analysis, Writing – original draft, Writing - review & editing. **Ganesh Balasubramanian:** Funding acquisition, Supervision, Resources, Writing - review & editing.

Declaration of Competing Interest

The authors declare that they have no known competing financial interests or personal relationships that could have appeared to influence the work reported in this paper.

Acknowledgment

The research was supported, in part, by the National Science Foundation (NSF) grant no. CMMI-1753770. The work at Ames Laboratory was supported by the U.S. Department of Energy (DOE), Office of Science, Basic Energy Sciences, Materials Science & Engineering Division, which is operated by Iowa State University for the U.S. DOE under contract DE-AC02-07CH11358.

Appendix A. Supplementary data

Supplementary data to this article can be found online at https://doi.org/10.1016/j.commatsci.2021.110823.

References

[1] O.A. Jaramillo-Quintero, R.S. Sanchez, M. Rincon, I. Mora-Sero, Bright Visible-Infrared Light Emitting Diodes Based on Hybrid Halide Perovskite with Spiro-OMeTAD as a Hole-Injecting Layer, J. Phys. Chem. Lett. 6 (2015) 1883–1890.
[2] Z.-K. Tan, et al., Bright light-emitting diodes based on organometal halide perovskite, Nat. Nanotechnol. 9 (2014) 687–692.
[3] X.Y. Chin, D. Cortecchia, J. Yin, A. Bruno, C. Soci, Lead iodide perovskite light-emitting field-effect transistor, Nat. Commun. 6 (1) (2015), https://doi.org/10.1038/ncomms8383.
[4] G. Xing et al. Long-Range Balanced Electron- and Hole-Transport Lengths in Organic-Inorganic CH3NH3PbI3. Science 342, 344–347 (2013).
[5] H.S. Jung, N.-G. Park, Perovskite Solar Cells: From Materials to Devices, Small 11 (1) (2015) 10–25.
[6] A. Kojima, K. Teshima, Y. Shirai, T. Miyasaka, Organometal Halide Perovskites as Visible-Light Sensitizers for Photovoltaic Cells, J. Am. Chem. Soc. 131 (2009) 6050–6051.
[7] Y. Ogomi et al. CH 3 NH 3 Sn x Pb (1– x) I 3 Perovskite Solar Cells Covering up to 1060 nm. J. Phys. Chem. Lett. 5, 1004–1011 (2014).
[8] H.J. Snaith, Perovskites: The Emergence of a New Era for Low-Cost, High-Efficiency Solar Cells, J. Phys. Chem. Lett. 4 (21) (2013) 3623–3630.
[9] T.-B. Song, et al., Perovskite solar cells: film formation and properties, J. Mater. Chem. A 3 (2015) 9032–9050.
[10] T.C. Sum, N. Mathews, Advancements in perovskite solar cells: photophysics behind the photovoltaics, Energy Env. Sci 7 (2014) 2518–2534.
[11] D. Weber, CH3NH3PbX3, ein Pb(II)-System mit kubischer Perowskitstruktur / CH3NH3PbX3, a Pb(II)-System with Cubic Perovskite Structure. Z. Für Naturforschung B 33, (1978).
[12] M. Sessolo, and H.J. Bolink, Perovskite solar cells join the major league. Science 350, 917–917 (2015).
[13] S.D. Stranks, H.J. Snaith, Metal-halide perovskites for photovoltaic and light-emitting devices, Nat. Nanotechnol. 10 (2015) 391–402.
[14] W.S. Yang et al. Iodide management in formamidinium-lead-halide–based perovskite layers for efficient solar cells. Science 356, 1376–1379 (2017).
[15] J. Berry et al. Hybrid Organic-Inorganic Perovskites (HOIPs): Opportunities and Challenges. Adv. Mater. 27, 5102–5112 (2015).

[16] J. Burschka et al. Sequential deposition as a route to high-performance perovskite-sensitized solar cells. Nature 499, 316–319 (2013).

[17] M.A. Green, A. Ho-Baillie, H.J. Snaith, The emergence of perovskite solar cells, Nat. Photonics 8 (7) (2014) 506–514.

[18] J.H. Heo et al. Efficient inorganic–organic hybrid heterojunction solar cells containing perovskite compound and polymeric hole conductors. Nat. Photonics 7, 486–491 (2013).

[19] X. Huang et al. High-performance transition metal-doped Pt3Ni octahedra for oxygen reduction reaction. Science 348, 1230–1234 (2015).

[20] J.-H. Im, I.-H. Jang, N. Pellet, M. Grätzel, N.-G. Park, Growth of CH3NH3PbI3 cuboids with controlled size for high-efficiency perovskite solar cells, Nat. Nanotechnol. 9 (2014) 927–932.

[21] D. Liu, T.L. Kelly, Perovskite solar cells with a planar heterojunction structure prepared using room-temperature solution processing techniques, Nat. Photonics 8 (2) (2014) 133–138.

[22] A. Mei et al. A hole-conductor-free, fully printable mesoscopic perovskite solar cell with high stability. Science 345, 295–298 (2014).

[23] C. Wehrenfennig, G.E. Eperon, M.B. Johnston, H.J. Snaith, L.M. Herz, High Charge Carrier Mobilities and Lifetimes in Organolead Trihalide Perovskites, Adv. Mater. 26 (2014) 1584–1589.

[24] A.G. Ricciardulli, S. Yang, J.H. Smet, M. Saliba, Emerging perovskite monolayers, Nat. Mater. (2021), https://doi.org/10.1038/s41563-021-01029-9.

[25] L. Dou et al. Atomically thin two-dimensional organic-inorganic hybrid perovskites. Science 349, 1518–1521 (2015).

[26] V.M. Goldschmidt, Die Gesetze der Krystallochemie. *Naturwissenschaften* 14 (21) (1926) 477–485.

[27] L. Ma, J. Dai, X.C. Zeng, Two-Dimensional Single-Layer Organic-Inorganic Hybrid Perovskite Semiconductors, Adv. Energy Mater. 7 (2017) 1601731.

[28] M. Pandey, K.W. Jacobsen, K.S. Thygesen, Bandgap Tuning and Defect Tolerance of Atomically Thin Two-Dimensional Organic-Inorganic Halide Perovskites, J. Phys. Chem. Lett. 7 (2016) 4346–4352.

[29] L.D. Hicks, M.S. Dresselhaus, Effect of quantum-well structures on the thermoelectric figure of merit, Phys. Rev. B 47 (1993) 12727–12731.

[30] W. Chen, S. Chen, D.C. Qi, X.Y. Gao, A.T.S. Wee, Surface Transfer p-Type Doping of Epitaxial Graphene, J. Am. Chem. Soc. 129 (2007) 10418–10422.

[31] A.J. Samuels, J.D. Carey, Molecular Doping and Bandgap Opening of Bilayer Graphene, ACS Nano 7 (3) (2013) 2790–2799.

[32] S. Mouri, Y. Miyauchi, K. Matsuda, Tunable Photoluminescence of Monolayer MoS_2 via Chemical Doping, Nano Lett. 13 (2013) 5944–5948.

[33] D. Kiriya, M. Tosun, P. Zhao, J.S. Kang, A. Javey, Air-Stable Surface Charge Transfer Doping of MoS_2 by Benzyl Viologen, J. Am. Chem. Soc. 136 (2014) 7853–7856.

[34] J.M.O. Zide, et al., Demonstration of electron filtering to increase the Seebeck coefficient in In 0.53 Ga 0.47 As / In 0.53 Ga 0.28 Al 0.19 As superlattices, Phys. Rev. B 74 (2006).

[35] S. Kohnehpoushi, P. Nazari, B.A. Nejand, M. Eskandari, MoS2: a two-dimensional hole-transporting material for high-efficiency, low-cost perovskite solar cells, Nanotechnology 29 (2018) 205201-.

[36] G. Kresse, J. Furthmüller, Efficiency of ab-initio total energy calculations for metals and semiconductors using a plane-wave basis set, Comput. Mater. Sci. 6 (1) (1996) 15–50.

[37] G. Kresse, J. Furthmüller, Efficient iterative schemes for *ab initio* total-energy calculations using a plane-wave basis set, Phys. Rev. B 54 (1996) 11169–11186.

[38] P.E. Blöchl, Projector augmented-wave method, Phys. Rev. B 50 (1994) 17953–17979.

[39] G. Kresse, J. Hafner, Ab initio molecular dynamics for liquid metals, Phys Rev B Condens Matter. 47 (1) (1993) 558–561.

[40] J.P. Perdew, K. Burke, and M. Ernzerhof, Generalized Gradient Approximation Made Simple, Phys. Rev. Lett. 77, 3865 (1996), ibid, Phys. Rev. Lett. 78, 1396–1396 (1997).

[41] H.J. Monkhorst, J.D. Pack, Special points for Brillouin-zone integrations, Phys. Rev. B 13 (1976) 5188.

[42] G.K.H. Madsen, D.J. Singh, BoltzTraP., A code for calculating band-structure dependent quantities, Comput. Phys. Commun. 175 (2006) 67–71.

[43] M. Gajdoš, K. Hummer, G. Kresse, J. Furthmüller, F. Bechstedt, Linear optical properties in the projector-augmented wave methodology, Phys. Rev. B 73 (4) (2006), https://doi.org/10.1103/PhysRevB.73.045112.

[44] M. Dion, H. Rydberg, E. Schröder, D.C. Langreth, B.I. Lundqvist, Van der Waals Density Functional for General Geometries, Phys. Rev. Lett. 92 (24) (2004), https://doi.org/10.1103/PhysRevLett.92.246401.

[45] G. Román-Pérez, J.M. Soler, Efficient Implementation of a van der Waals Density Functional: Application to Double-Wall Carbon Nanotubes, Phys. Rev. Lett. 103 (9) (2009), https://doi.org/10.1103/PhysRevLett.103.096102.

[46] I. Hamada, van der Waals density functional made accurate, Phys. Rev. B 89 (12) (2014), https://doi.org/10.1103/PhysRevB.89.121103.

[47] S.D. Stranks et al. Electron-Hole Diffusion Lengths Exceeding 1 Micrometer in an Organometal Trihalide Perovskite Absorber. Science 342, 341–344 (2013).

[48] T. Leijtens et al. Stability of Metal Halide Perovskite Solar Cells. Adv. Energy Mater. 5, 1500963 (2015).

[49] F. Brivio et al. Lattice dynamics and vibrational spectra of the orthorhombic, tetragonal, and cubic phases of methylammonium lead iodide. Phys. Rev. B 92, (2015).

[50] F. Brivio, A.B. Walker, A. Walsh, Structural and electronic properties of hybrid perovskites for high-efficiency thin-film photovoltaics from first-principles, APL Mater. 1 (2013), 042111.

[51] T. Baikie et al. Synthesis and crystal chemistry of the hybrid perovskite (CH3NH3) PbI3 for solid-state sensitised solar cell applications. J. Mater. Chem. A 1, 5628 (2013).

[52] P. Nandi, et al., $CH_3NH_3PbI_3$, A Potential Solar Cell Candidate: Structural and Spectroscopic Investigations, J. Phys. Chem. A 120 (2016) 9732–9739.

[53] X. Lu et al. First-principles insight into the photoelectronic properties of Ge-based perovskites. RSC Adv. 6, 86976–86981 (2016).

[54] Z.-K. Tang et al. Enhanced optical absorption via cation doping hybrid lead iodine perovskites. Sci. Rep. 7, (2017).

[55] Z. Fan, et al. Layer-by-Layer Degradation of Methylammonium Lead Tri-iodide Perovskite Microplates. Joule 1, 548–562 (2017).

[56] Y. Li, Y.-L. Li, C.M. Araujo, W. Luo, R. Ahuja, Single-layer MoS2 as an efficient photocatalyst, Catal. Sci. Technol. 3 (2013) 2214.

[57] R. Kim, M.S. Lundstrom, Computational study of the Seebeck coefficient of one-dimensional composite nano-structures, J. Appl. Phys. 110 (2011), 034511.

[58] C. Kittel, Introduction to Solid State Physics. (Wiley).

[59] A.F. Ioffe et al. Semiconductor Thermoelements and Thermoelectric Cooling. Phys. Today 12, 42–42 (1959).

[60] R. Singh, R. Kottokkaran, V.L. Dalal, G. Balasubramanian, Engineering Bandgap and Electronic Transport in Organic-Inorganic Halide Perovskites by Superlattices, Nanoscale 9 (25) (2017) 8600–8607.

[61] M.-G. Ju, J. Dai, L. Ma, X.C. Zeng, Perovskite Chalcogenides with Optimal Bandgap and Desired Optical Absorption for Photovoltaic Devices, Adv. Energy Mater. 7 (2017) 1700216.

[62] Z. Fan, et al. Layer-by-Layer Degradation of Methylammonium Lead Tri-iodide Perovskite Microplates. Joule 1, 548–562 (2017).